States of stress and slip partitioning in a continental scale strike-slip duplex: Tectonic and magmatic implications by means of finite element modeling

Pablo Cristián Iturrieta [a,b,*], Daniel E. Hurtado [a], José Cembrano [a,b], Ashley Stanton-Yonge [a,b]

[a] *Department of Structural and Geotechnical Engineering, School of Engineering, Pontificia Universidad Católica de Chile, Vicuña Mackenna 4860, Macul, Santiago, Chile*
[b] *Andean Geothermal Centre of Excellence (CEGA), Universidad de Chile, Plaza Ercilla 803, Santiago, Chile*

A R T I C L E   I N F O

A B S T R A C T

Orogenic belts at oblique convergent subduction margins accommodate deformation in several trench-parallel domains, one of which is the magmatic arc, commonly regarded as taking up the margin-parallel, strike-slip component. However, the stress state and kinematics of volcanic arcs is more complex than usually recognized, involving first- and second-order faults with distinctive slip senses and mutual interaction. These are usually organized into regional scale strike-slip duplexes, associated with both long-term and short-term heterogeneous deformation and magmatic activity. This is the case of the 1100 km-long Liquiñe–Ofqui Fault System in the Southern Andes, made up of two overlapping margin-parallel master faults joined by several NE-striking second-order faults. We present a finite element model addressing the nature and spatial distribution of stress across and along the volcanic arc in the Southern Andes to understand slip partitioning and the connection between tectonics and magmatism, particularly during the interseismic phase of the subduction earthquake cycle. We correlate the dynamics of the strike-slip duplex with geological, seismic and magma transport evidence documented by previous work, showing consistency between the model and the inferred fault system behavior. Our results show that maximum principal stress orientations are heterogeneously distributed within the continental margin, ranging from 15° to 25° counter-clockwise (with respect to the convergence vector) in the master faults and 10–19° clockwise in the forearc and backarc domains. We calculate the stress tensor ellipticity, indicating simple shearing in the eastern master fault and transpressional stress in the western master fault. Subsidiary faults undergo transtensional-to-extensional stress states. The eastern master fault displays slip rates of 5 to 10 mm/yr, whereas the western and subsidiary faults show slips rates of 1 to 5 mm/yr. Our results endorse that favorably oriented subsidiary faults serve as magma pathways, particularly where they are close to the intersection with a master fault. Also, the slip of a fault segment is enhanced when an adjacent fault kinematics is superimposed on the regional tectonic loading. Hence, finite element models help to understand coupled tectonics and volcanic processes, demonstrating that geological and geophysical observations can be accounted for by a small number of key first order boundary conditions.

© 2017 Elsevier B.V. All rights reserved.

1. Introduction

Regional crustal stress in convergent margins is commonly compartmentalized as faults with various orientations within the continental lithosphere. Faults locally disrupt the stress field,

* Corresponding author at: Department of Structural and Geotechnical Engineering, School of Engineering, Pontificia Universidad Católica de Chile, Vicuña Mackenna 4860, Macul, Santiago, Chile.
E-mail address: pciturri@uc.cl (P.C. Iturrieta).

where the variation of stress orientations and relative magnitudes lead to different mechanisms of seismic faulting and fluid migration (e.g. Nakamura et al., 1977; Rubin, 1995; Sibson, 1994), which uses conduits located in not only brittle, but also ductile shear zones (e.g. Hutton, 1988). Furthermore, brittle faulting occurs near the surface, typically under the Mohr–Coulomb criterion, whereas thermo-activated crystal–plastic deformation mechanisms take place as depth and temperature increases (McClay, 1977; Tullis and Yund, 1987). These mechanisms include, but are not

limited to, dislocation creep (climb and glide) beneath the brittle-plastic transition and diffusion creep (e.g. Cobble and Nabarro-Herring creep, both sensitive to grain-size) in deeper structural levels. However, the precise relationship between magma transport and deformation mechanisms in plastic shear zones (i.e. beneath the seismogenic region) remains speculative. It is established that a strong dependence on viscosity contrast between host rock and magma composition should be taken into account of such relationship (Rubin, 1995). While seismic pumping is capable to transporting large volumes of magma, crystal–plastic mechanisms in mylonites develop large, low-permeability crack networks that could serve as magma transport conduits (e.g. Bauer et al., 2000). Therefore, regardless of the transport mechanism, local extension must exist (at least down to the intrinsic length scale of plasticity) for magma to migrate, thus ensuring kinematic compatibility.

In this context, transcurrent fault systems are large-scale shear zones that cut through the lithosphere, generally driven by oblique plate convergence. They are composed of a series of anastomosed faults striking sub-parallel to the plate margin, thus accommodating a significant part of the convergence margin-parallel component (Teyssier et al., 1995). Also, they are commonly arranged in two or more conjugate sets of opposite-verging faults (e.g. Braun and Beaumont, 1995), which could be connected by second-order structures: such is the case of strike-slip duplexes (Woodcock and Fischer, 1986).

An outstanding case study of a regional-scale transcurrent shear zone, is the Liquiñe–Ofqui Fault System (LOFS) (Fig. 1), which is located within the South-Andean margin. It runs over 1100 km from south of the Ofqui isthmus (48°S) to Alto Bio-bio (37°S) (e.g Melnick et al., 2006). The LOFS is described as a long lived intra-arc structure that has been active – at least – since 6 Ma (Cembrano et al., 2002). Geological evidence (e.g. Arancibia et al., 1999; Lavenu and Cembrano, 1999), along with seismic (Lange et al., 2008) and geodetic observations (Wang et al., 2007) documents its overall transpressional dextral kinematics.

The LOFS deformation is genetically associated and kinematically consistent with: (i) NNE and NE alignments of volcanic centers (Nakamura et al., 1977; Cembrano and Lara, 2009); (ii) sharp geomorphic lineaments, where faulting contributed to the landscape evolution by differential erosion since the Pliocene (Cembrano et al., 1996; Glasser and Ghiglione, 2009); (iii) high denudation rates (1 mm/yr) due to the balance between transpressional surface uplift and high glacial erosion rates (Thomson, 2002); (iv) shallow seismicity (<10 km) (Cembrano and Lara, 2009; Lange et al., 2008; Legrand et al., 2011); and (v) active hydrothermal reservoirs and fault-vein networks associated with paleofluid flow (e.g. Sánchez et al., 2013). Hence, the importance of studying LOFS deformation goes from fundamental tectonics to hazard assessment and geothermal potential.

The LOFS present-day interplay between tectonics and magma transport was clearly documented during the Aysén duplex seismic swarm in 2007 (Lange et al., 2008; Legrand et al., 2011). Thousands of earthquakes occurred within the duplex domain, ending in two large events of magnitudes $M_w = 6.1$ and $M_w = 6.2$, see Fig. 1. The first event was both volcanic and tectonically driven with normal-extensional focal mechanism, most likely caused by dike upward propagation. This event subsequently activated a LOFS master fault in a second seismic event, displaying a well-constrained strike-slip focal mechanism. However, the stress state and kinematic regimes at the brittle–plastic transition, right beneath where the seismic swarm was nucleated (8–10 km), are still poorly understood.

In this work, we examine the stress and deformation fields at the LOFS strike-slip duplex within the brittle–plastic transition using numerical simulations. Our main goal is to understand the interaction between adjacent fault segments of a strike-slip du-
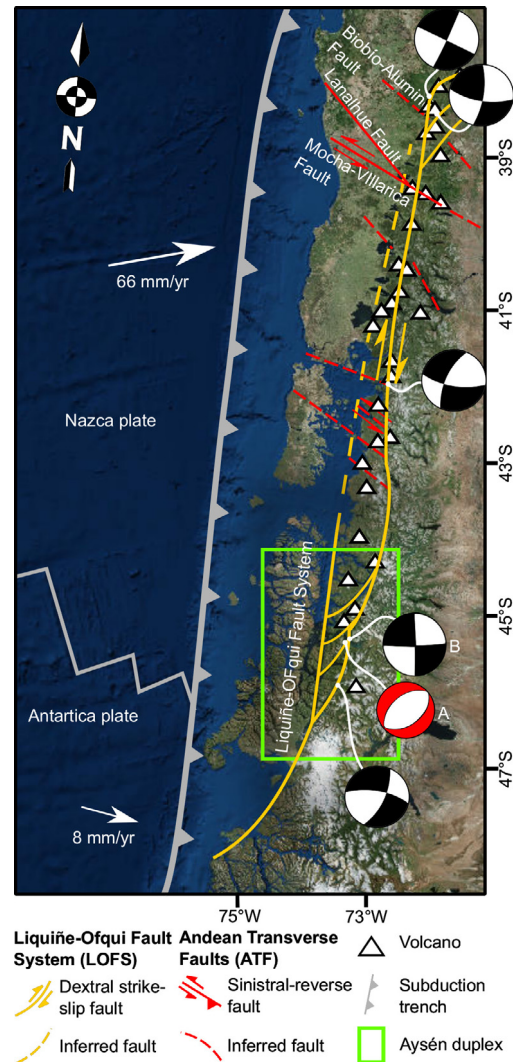

Fig. 1. Tectonic setting showing the main strands of the LOFS within the South-Andean margin. Andean Transverse Faults [ATF] are shown in red (modified from Sánchez et al., 2013), along with representative stratovolcanoes of the volcanic arc. The southern Aysén duplex is highlighted in the green frame. Main historical focal mechanisms of the LOFS are shown (Lange et al., 2008) along with the Aysén swarm culminating events (**A** represents the 3/02/2007 $M_w = 6.1$ extensional earthquake and **B** the 3/21/2007 $M_w = 6.2$ strike-slip earthquake) (Legrand et al., 2011). (For interpretation of the references to color in this figure legend, the reader is referred to the web version of this article.)

plex and suitable tectonic settings for magma upward migration; particularly, we estimate the steady-state stress-field acting on the LOFS current geometry, and use it as a basis for detecting favorable fluid transport conditions. Further, we calculate the velocity field within the continental lithosphere and slip rates of the LOFS duplex segments, to answer open questions such as: How is slip partitioned along and across the continental margin and why? What are the LOFS slip rates and their distribution along strike? To this end, we develop a finite element model (FEM) of the LOFS duplex that reproduces a horizontal slice of the continental lithosphere at and beneath the brittle–plastic transition. Using a continuum-mechanics formulation that considers elastoplastic material behavior, we model the LOFS duplex geometry (i.e. structures are represented as volumes rather than discontinuities) and the surrounding wallrock. To validate our numerical model, we confront our results with seismic and geological data recorded in the field.

2. Geotectonic framework

The tectonics of the Andes Southern Volcanic Zone is controlled by convergence and subduction between the Nazca and South-American plates. The Peru–Chile trench trends N10°E, whereas the convergence velocity vector trends N80°E at 66 mm/yr (Anger-mann et al., 1999) (Fig. 1). This obliquity angle ($\approx 20°$ counter-clockwise) has remained roughly the same for the last 10 Ma (Kendrick et al., 2003; Argus et al., 2010) and is sufficient for slip partitioning to partially occur within the Southern Andes intra-arc (Arancibia et al., 1999; Lavenu and Cembrano, 1999; Stanton-Yonge et al., 2016). However, south of the Chilean Triple Junction (be-tween Nazca, South-America and Antarctica plates at 46° latitude), convergence between Antarctica and South America is mainly or-thogonal to the trench (DeMets et al., 2010).

Several oblique-to-the-arc faults are found along the LOFS (Cembrano and Lara, 2009). They consist either of secondary struc-tures splaying off the LOFS or ancient basement inherited faults (e.g. Stanton-Yonge et al., 2016, and references therein). The lat-ter have been grouped into the so-called Andean Transverse Faults [ATF] (shown in red in Fig. 1). Most of them are cut and/or dis-placed by the LOFS master faults. In the northern end of the LOFS, a horse-tail structure is displayed (Melnick et al., 2006; Pérez-Flores et al., 2016), whereas in the south, two large NNE-trending master faults form a strike-slip duplex at a right step-over (Cembrano et al., 1996) (Fig. 1). The latter is located within the Aysén fjord (44–46°S), where quartz-feldspathic mylonitic rocks and upper crustal faults have been exhumed from depths of a few kilometers. Both document compressional to transpressional defor-mation events (Arancibia et al., 1999; Lavenu and Cembrano, 1999; Vargas et al., 2013).

The LOFS duplex runs mostly through the North Patagonian batholith, consisting of Late Cenozoic granitoids, which intrude Pa-leozoic metamorphic complexes (Hervé, 1993) and Early Cenozoic volcano-sedimentary rocks (Hervé et al., 1995). Within the LOFS domain, plastic deformation localizes in discrete anastomosed my-lonitic rock bands, with widths ranging from 1 cm to 1 m. They are distributed within large encompassing fault zones, whose total width may reach up to 4 km (Cembrano et al., 1996). The du-plex consists of two master faults that dip towards each other at a right step-over, thus suggesting a palm-tree geometry (Thomson, 2002). Similar steep dips documented on brittle-faults and my-lonitic bands (Arancibia et al., 1999; Cembrano et al., 2002; Vargas

et al., 2013) suggest the continuity of this geometry, at least down to the brittle–plastic transition (Fig. 2). However, the distance be-tween both master faults at the surface (≈ 40 km), along with their steep dips, implies that the master faults should not coalesce at the brittle–plastic transition (8–11 km depth), in opposition to what was suggested by Thomson (2002). Therefore, constraints set by the duplex geometry at the surface, the observed fault dip and crustal seismicity could only be attainable if the coalescing point were well underneath the brittle–plastic transition. One signifi-cant, independent evidence for the LOFS master faults depth is provided by a series of monogenetic volcanic cones built on top of surface fault traces (Lara et al., 2008). The mantelic geochemi-cal signature of the magmas suggests they were transported at a geologically instantaneous rate along sub-vertical paths from the underlying asthenosphere (Cembrano and Lara, 2009). Moreover, numerical simulations of strain partitioning across transpressional plate boundaries in transcurrent shear zones (Braun and Beau-mont, 1995) suggest such master faults should coalesce close to the asthenospheric wedge.

3. Methodology

To address the mechanics of the LOFS, we consider an elasto-plastic continuum formulation, which is solved using a finite-element numerical scheme, as is detailed next.

3.1. Continuum governing equations

We consider the crust and LOFS domain as a continuum solid, which must satisfy the linear-momentum balance principle. As-suming a quasi-static problem, we neglect inertial terms, and the balance equations reduce to the differential equilibrium equation

$$\nabla \cdot \boldsymbol{\sigma} + \rho \boldsymbol{g} = \boldsymbol{0}, \tag{1}$$

where bold fonts are used to represent vectors and tensors and normal fonts to represent scalars, $\boldsymbol{\sigma}$ is the Cauchy stress tensor, $\nabla \cdot ()$ represents the divergence operator, ρ is the rock density, and $\boldsymbol{g}$ is the gravity vector field. Let $\boldsymbol{u}(\boldsymbol{x})$ be the displacement field, then the strain tensor is $\boldsymbol{\varepsilon} = 1/2(\nabla \boldsymbol{u} + \nabla \boldsymbol{u}^t)$, where $\nabla ()$ is the gradient operator. To account for elastic–plastic behavior, we de-compose the strain tensor into its elastic strain and plastic strain components, represented by $\boldsymbol{\varepsilon}^e$ and $\boldsymbol{\varepsilon}^p$, respectively, and write

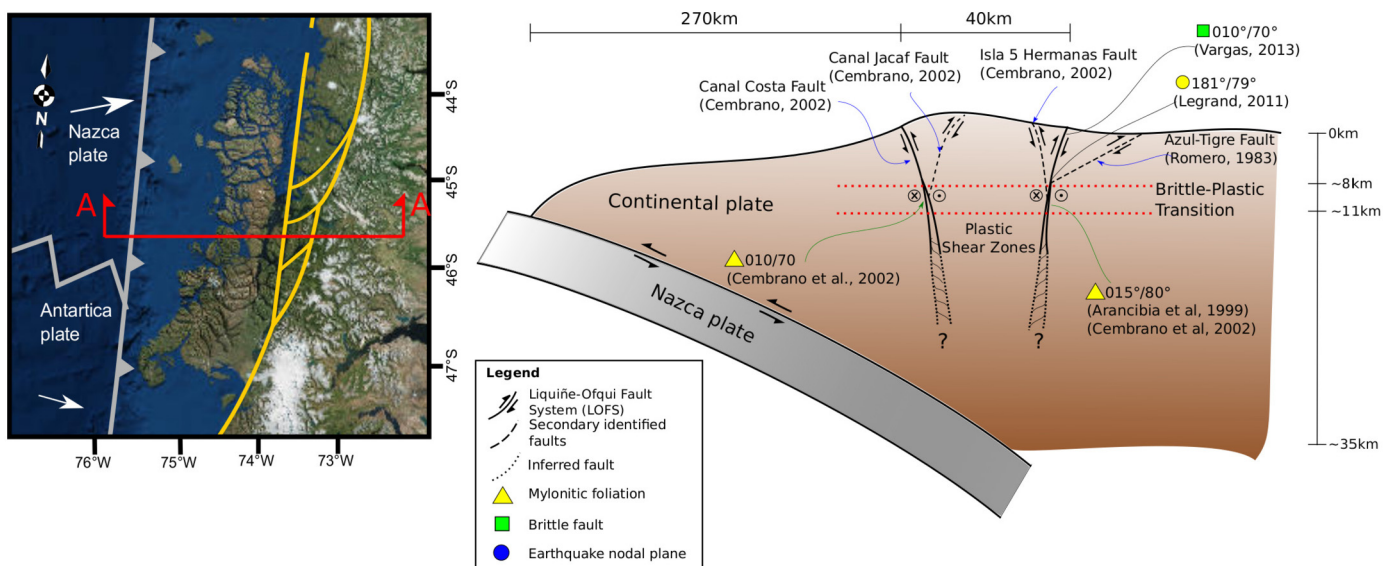$$\boldsymbol{\varepsilon} = \boldsymbol{\varepsilon}^e + \boldsymbol{\varepsilon}^p. \tag{2}$$

Fig. 2. Schematic vertical section of the continental lithosphere in orientation A–A. Previous work data and field mapping are projected in a representative LOFS section.

Then, the stress is defined in terms of the elastic strain:

$$\boldsymbol{\sigma} = \boldsymbol{C} : \boldsymbol{\varepsilon}^e, \tag{3}$$

where the operator : denotes a tensor contraction and $\boldsymbol{C}$ is the fourth-order elasticity tensor, assumed to be isotropic. It is useful to refer to the plastic behavior by defining the effective plastic strain

$$\underline{\varepsilon}^p = \sqrt{\frac{2}{3}\boldsymbol{\varepsilon}^p : \boldsymbol{\varepsilon}^p} \tag{4}$$

Throughout this work, which addresses the mechanical state in the brittle–plastic transition, we consider a yield criterion and flow law dependent of plastic strain ($\underline{\varepsilon}^p$) and pressure-independent (p). The implications of this particular choice will be further discussed in Section 5.1. We define the deviatoric stress tensor by $\boldsymbol{s} = \boldsymbol{\sigma} - p\boldsymbol{I}$ and the effective deviatoric stress as

$$\underline{\sigma} = \sqrt{\frac{1}{2}\boldsymbol{s} : \boldsymbol{s}}. \tag{5}$$

Plastic behavior onset in the solid media is determined by the yield function $\varphi(\boldsymbol{\sigma}, \boldsymbol{\varepsilon}^p)$, which for a von-Mises yield criterion takes the form

$$\varphi(\boldsymbol{\sigma}, \boldsymbol{\varepsilon}^p) = \underline{\sigma} - \tau_y(\underline{\varepsilon}^p) \le 0, \tag{6}$$

where τ_y represents the critical shear strength, which evolves according to the exponential hardening law (Voce, 1955).

$$\tau_y(\underline{\varepsilon}^p) = \tau_\infty + (\tau_0 - \tau_\infty)\exp(-\beta\underline{\varepsilon}^p). \tag{7}$$

Here, τ_0 represents the initial shear strength, and τ_∞ the saturation shear strength, whereas β is a hardening exponential rate. Although this is a general approximation, it is commonly used to describe the strain-hardening stage of geomaterials, through the homogenization of a fractured rock mass (e.g. Pouya and Ghoreychi, 2001). Summarizing, equations (1), (2), (3), (6) and (7) represent a set of partial differential equations, which along boundary conditions for the displacements and tractions constitute an initial boundary value problem.

3.2. Finite element model

To numerically solve the governing initial boundary value problem, we propose to use the finite element method for an elastic–plastic material formulation (de Souza Neto et al., 2011), where a Lagrangian framework is assumed. For a complete treatment of finite element formulations in solid mechanics the reader is referred to Zienkiewicz and Taylor (2000). As a first step, a 3D discretization of the domain was generated to obtain a tetrahedral mesh. It represents a horizontal 1 km-thick slice of the continental lithosphere, in which we included the LOFS geometry at the brittle–plastic transition. Two different setups were considered: one at 10 km depth and the other at 15 km. Fig. 3 shows the model representation of the continental lithosphere encompassing the LOFS duplex 400 km east of the trench, with a 400 km length along the NS axis. Dimensions of the model were extended away of the strike-slip duplex, to minimize the influence of boundary conditions on the distribution of deformation in and around the fault duplex. The model was built by first meshing the domain with coarse elements. The mesh was adaptively refined towards the fault system, where a finer mesh is required to better reflect the geometry and increase the numerical accuracy of the FE solution. The mesh-generation process was performed using ANSYS Meshing 15.0, creating a total of $1.3 \cdot 10^6$ elements with a mean and maximum of 1.14 and 3.96 radius ratio, respectively.

Three regions with different material properties were considered within the model domain: host rock, pop-up blocks and fault
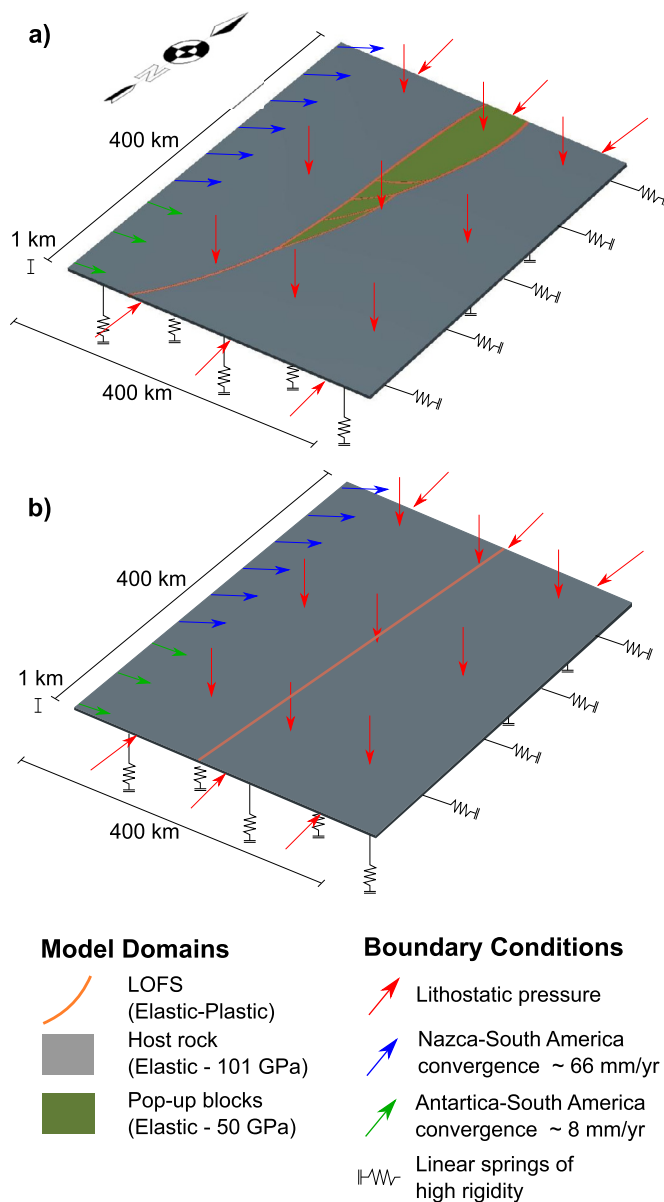

Fig. 3. Domains spatial distribution and boundary conditions used in the models. Model (a) represents the LOFS at 10 and 15 km depth and its boundary conditions. Model (b) is an equivalent single-fault model, using the same material properties and boundary conditions than model (a).

zone rocks; see Fig. 3. The elastic modulus E and Poisson's ratio ν of the host rock were set to 101 GPa and 0.25 respectively, calculated using a density of $\rho = 2800$ km/m^2 and P-wave velocity of $V_p = 6.6$ km/s. These values were obtained from a regional gravity survey (Introcaso et al., 1992) and seismic refraction (Barrientos et al., 2004) performed in the southern Andes continental margin. The domain encompassed by the LOFS master faults is referred to as pop-up blocks, which is distinguished from the forearc and backarc host rock by decreasing its Young modulus to 50 GPa. The latter is an attempt to represent its more fractured state due to recurrent faulting, while still behaving elastically at a macroscopic scale. The increased thermal gradient in the volcanic arc, where the pop-up blocks are located, also supports this elastic stiffness reduction, since the value of E diminishes with temperature. We modeled the fault zone using an elastic–plastic constitutive relation, following a von-Mises yield criteria as defined in Equation (6) and Equation (7). Similar approaches can be found in

Regenauer-Lieb and Yuen (1998), Hardacre and Cowie (2003). Its elastic properties are equal to those of the pop-up blocks. The values of τ_0 and τ_∞ were set to 20 MPa and 8 MPa respectively, to represent the range of experimentally deformed mylonites (White et al., 1980). The hardening exponential rate β was set to 100, intended to modulate the quick asymptotic behavior of τ_y between $\underline{\varepsilon}^p = 0$ and 0.05.

Steady-state loading was employed to represent the long-term deformation of the LOFS. This assumption is supported by the fact that we include in the geometry a developed shear zone, without considering its genesis. The model's boundary conditions were represented by an imposed velocity on its western surface simulating plate convergence. Linear springs of high stiffness were placed as a lateral constraint, reproducing the roughly null velocity condition caused by the entire South-American plate weight to the west, but neglecting stress concentration on the model's edges. The overburden pressure was simulated by weight body forces in each element and an uniform pressure on the model's top surface. Linear springs were attached to the bottom of the model to simulate the buoyancy effect of the underlying lower crust and mantle. Northern and southern free edges were laterally loaded according to the overburden pressure at the modeled depth. Since this is a 3D model, uplifting of the pop-up blocks should naturally occur in the interior of the analyzed domain. Whereas vertical stress and infinitesimal strain are modeled properly, fault dip-slip may be overestimated. This is because strain should be integrated through depth of the entire fault system geometry (e.g. splay faults in the brittle domain (Fig. 2)), which is beyond the scope of this work.

The model constructed here is intended to represent the inter-seismic phase of the subduction seismic cycle, when most of the permanent long-term geological deformation is achieved. One obvious limitation of this approach is that the region under study is currently in the post-seismic phase of the 1960 $M_w = 9.5$ Valdivia earthquake (Wang et al., 2007; Moreno et al., 2011). However, with our model we do not intend to reproduce the short-term current state of stress of the upper plate following any given earthquake, but instead we address the long-term state of stress in an obliquely converging continental margin in general.

The model setup also implies full inter-plate coupling throughout the subduction boundary. Again, this is a strong assumption as it is well known that current plate coupling is not only partial, but heterogeneously distributed across and along the plate interface (Moreno et al., 2011; Métois et al., 2012). Consistently with what we stated in the paragraph above, our model does not seek to reproduce the state of stress arising from the current nature of plate coupling, but for the more general, simple case, of homogeneous full plate coupling. One consequence of this is that our model will not necessarily reproduce the present-day state of stress at any given point, nor the exact slip-rate magnitudes, but rather the long-term general nature and spatial distribution of stresses along and across the continental margin.

After the mesh was generated, and the boundary conditions and loads were defined, we solved the set of nonlinear equations that depend on the nodal displacement values deforming the mesh grid. To this end, we used an enhanced version of FEAP 8.4.1.d, which uses iterative non-linear solvers to compute the nodal displacements. Post-processing data to generate stress and strain fields was performed using Paraview 4.0.1.

4. Results

The maximum and minimum compressional principal-stress axes orientation, σ_1 and σ_3, respectively, are shown as crosses in Fig. 4. An overall transpressional–compressional regime is generated within the domain of analysis, with horizontal σ_1 trend-ing from ESE–WNW to NE–SW. The principal orientations are heterogeneously oriented across and along the continental margin, having a strong dependence upon the rheological domain. In general, σ_1 orientations are not parallel to the convergence vector, but clockwise rotated outside the duplex faults and counter-clockwise rotated within them. Clockwise rotation attains 5° to 19° in the forearc and backarc domains, with an average value of 12°. Counter-clockwise rotations can attain as much as 25° in the master faults. The eastern master fault displays a more oblique orientation of σ_1 than that of its western counterpart. Secondary faults exhibit a σ_1 orientation of 0° to −12° with respect to the convergence vector.

As with σ_1, σ_3 axis orientations are mostly horizontal in the duplex faults (with the exception of the western master fault, where it becomes oblique as it extends to the north). This indicates an overall strike-slip stress state. In contrast, σ_3 orientations are mostly vertical in the forearc and pop-up blocks, indicating a compressional regime. Comparatively, σ_3 orientations become horizontal in the foreland, up to 50 km east from the duplex, beyond which its orientation progressively returns to the vertical. No significant differences in σ_1 and σ_3 axes orientations spatial distribution are yielded in the equivalent 15 km-depth model.

We characterize stress relative magnitudes using the stress shape ratio, which is an adimensional parameter defined as

$$\phi = \frac{\sigma_2 - \sigma_3}{\sigma_1 - \sigma_3}, \tag{8}$$

where σ_i denotes the i-th principal stress ($i = 1, 2, 3$) of the Cauchy stress tensor. The stress shape ratio enables contrast of different stress styles, such as the transtensional and transpressional states in a strike-slip context. A schematic representation of ϕ is shown in Fig. 5, explaining its associated stress states using the Mohr's circle.

The modeled stress shape ratio ϕ, at two depths of 10 km and 15 km, is shown in Fig. 6. In the 10 km-depth model, transpressional stress dominates the western master fault (with average values of $\phi = 0.2$), whereas pure strike-slip is shown in the eastern master fault (with ranging values of 0.5). A transtensional-to-extensional regime is produced in secondary NE striking faults, with a tendency towards strike-slip from south to north. In the 15 km-depth model the eastern master fault becomes more transpressional, whereas the western master fault becomes compressional. Secondary NE-striking faults transtensional domains become smaller than those of the 10 km-depth model. Their general stress state at the 15 km-depth model is strike-slip-to-transpressional.

The modeled slip rate within the different faults making up the duplex is calculated using the relative velocities of two small parallel segments, which face each other from both sides of the duplex fault under consideration. The slip rate field in [mm/yr] of the LOFS is plotted in Fig. 7. Fault segments display markedly different slip rates: The single southernmost segment has significant greater slip rate than the rest. It is followed in decreasing order of slip rate, by the eastern master fault and the secondary faults, and then the western master fault segment. The slip rate of the eastern master fault slightly increases northward, whereas the western master fault and secondary faults decrease in slip rate towards the north. In contrast, the single fault model displays an uniform slip rate of 16.6 mm/yr.
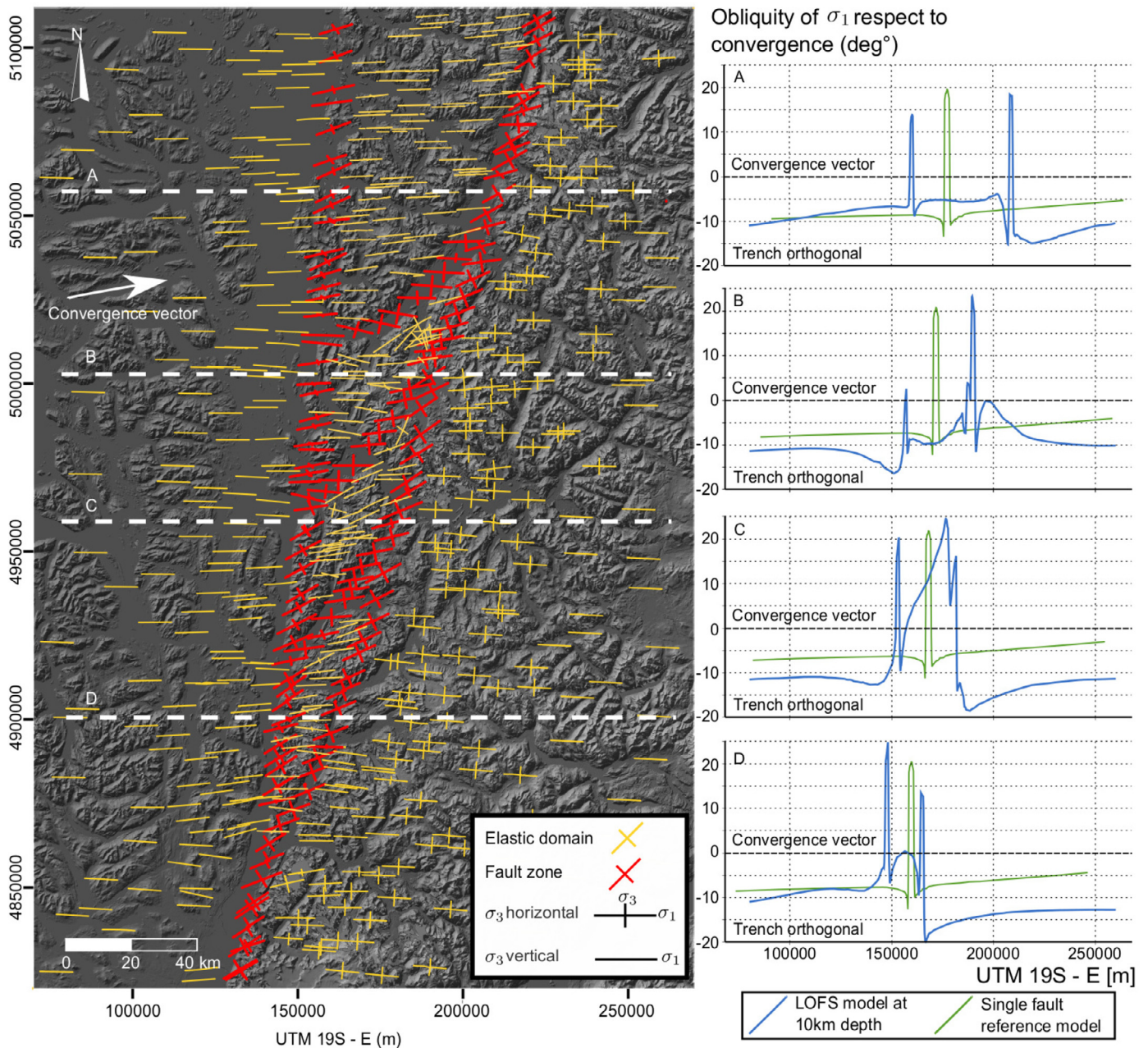
Fig. 4. Maximum (σ_1) and minimum (σ_3) principal stress orientations are projected as crosses to an horizontal plane at 10 km depth, where the large lines represents σ_1 and the small line represents σ_3. Given that σ_3 is not always horizontal, a strike-slip stress regime is exhibited when the full cross is plotted and a compressional regime is attained when only σ_1 is displayed. An oblique orientation (between the horizontal plane and the vertical axis) is attained where σ_3 is partially displayed. Red and yellow crosses represent the stress orientations within the fault system and over the outer/inner blocks, respectively. Segmented white line transects are displayed on the map, on which the obliquity of σ_1 orientation is plotted with respect to the convergence vector (N80°E). (For interpretation of the references to color in this figure legend, the reader is referred to the web version of this article.)

5. Discussion

5.1. Geological scope of the model

To model the deformation mechanisms within the entire fault zone, we make an effort to constrain the internal bulk plasticity of the rock volume rather than considering each individual shear band as a surface of discontinuity, such as in dislocation type models (e.g. Stanton-Yonge et al., 2016; Provost et al., 2003). Approaches similar to ours can be found in models of fabric development with prescribed plastic shear bands, using a von-Mises yield criterion to simulate dislocation glide (e.g. Schmalholz and Maeder, 2012), which is pressure independent. Furthermore, our

approach gives the outstanding advantage to account for the compartmentalization of stress and strain within the fault zone, rather than its localization in a discrete fault plane, which is not geologically accurate when representing the brittle–plastic transition. Another approach to model a fault zone consists in defining elastic volumes with reduced Young's modulus, which neglect permanent deformation produced by plastic flow (Karaoğlu et al., 2016). Since no yield stress limit is imposed in this method, it overestimates the stress field magnitude as it ignores the stress release when the fault zone slips (i.e. the stress strongly depends on the time of loading).

Permanent deformation in a fault zone is possible due to crystal–plastic slip systems, which is the main deformation mech-
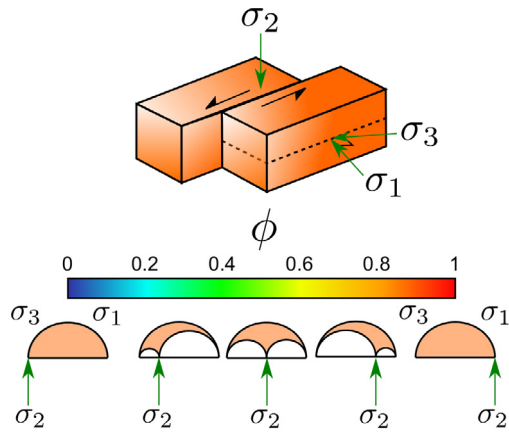
Fig. 5. Graphical representation of the stress shape ratio in an overall strike-slip regime. Values of $\phi = 0$ indicate uniaxial compression, $\phi = 0.5$ pure strike slip and $\phi = 1$ implies uniaxial extension. Transpression and transtension are located between those values, respectively.

anism in the brittle–plastic transition for quartz-rich rocks (Hirsch and Roberts, 1997; Hirth and Tullis, 1992), coexisting with microfracturing and pressure solution. We use a continuum approximation and a distributed plastic material model, characterized by a von-Mises criterion with isotropic strain-hardening. This is generally a common approach to model the brittle–plastic transition deformation mechanisms in shear zones, as suggested by Mancktelow (2006) and Regenauer-Lieb and Yuen (2003). However, there is a current uncertainty in the precise geometry of mylonitic shear bands throughout the fault system, along with the spatial distribution of its thermodynamic state (e.g. horizontal distribution of temperature, which activates plastic mechanisms). Therefore, we propose that the use of Von-Mises continuum plasticity approach is reasonable, given that it is able to reflect the average behavior of the fault zone. Its associated flow law allows strain to localize in the maximum shear stress direction, in contrast to a Mohr–Coulomb criterion. More complex constitutive relations can be used in future efforts, such as multi-scale plasticity models embedded in FE simulations (Hurtado and Ortiz, 2013), to account for dislocation, micro-fracturing and grain boundary deformation
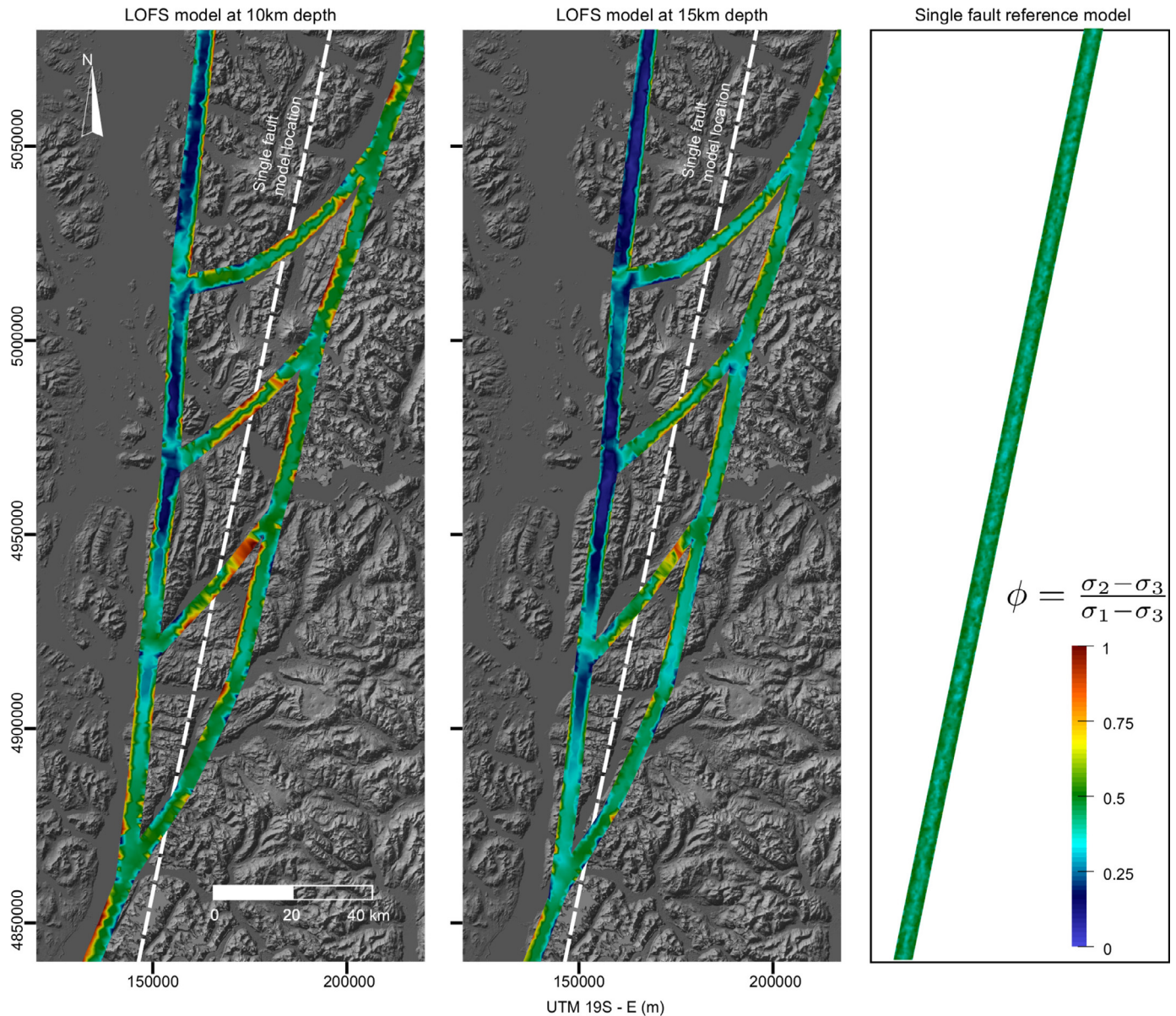

Fig. 6. Spatial distribution of the stress shape ratio throughout the fault system at 10 km depth and 15 km depth. It is also plotted for the single fault reference model.
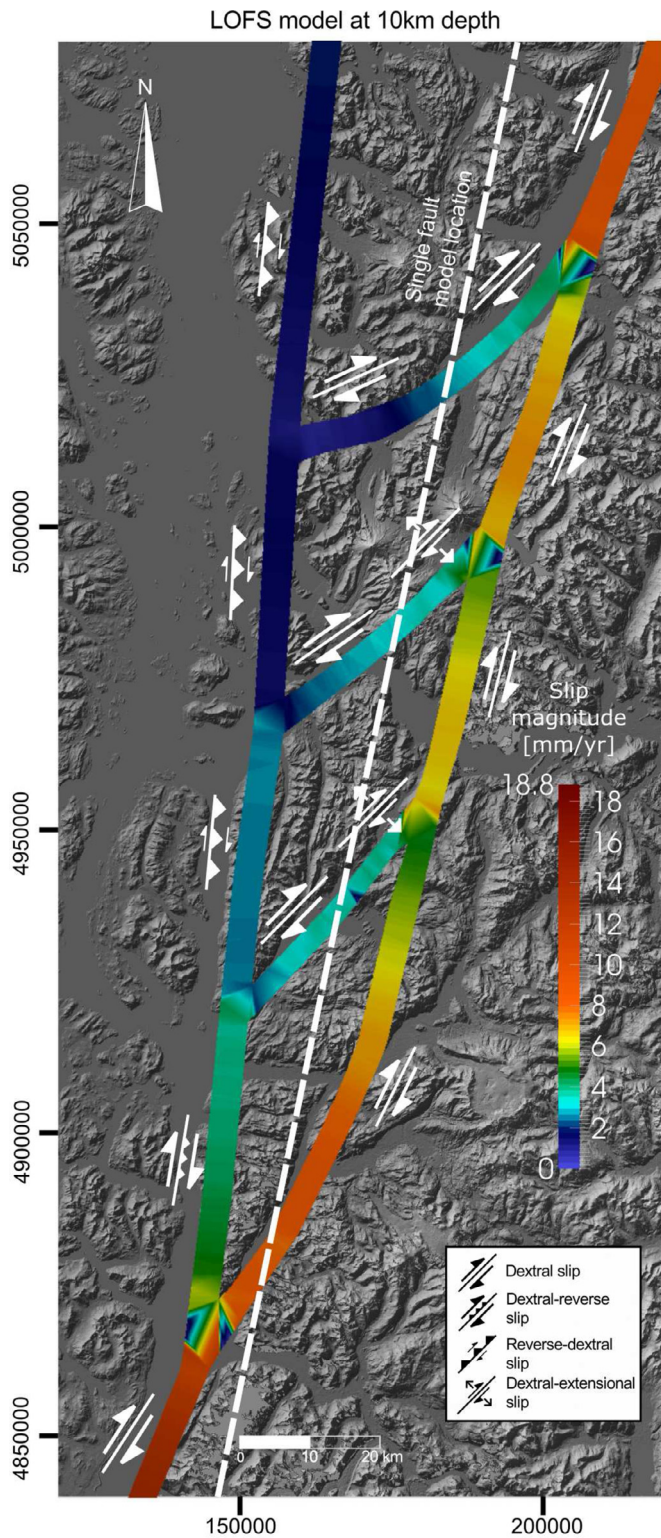
Fig. 7. Fault slip rate at master and subsidiary LOFS duplex faults. Slip rates within the duplex structures range from 1 to 10 mm per yr. The maximum slip rate is located in the southernmost single segment. The single fault model displays an uniform slip rate of 16.6 mm per yr. The overall kinematics of the duplex fault segments is displayed alongside.
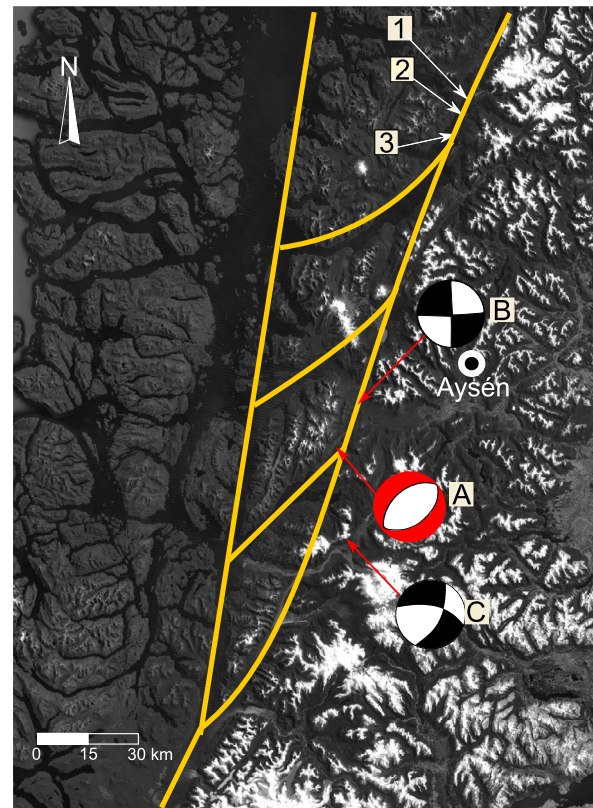
Fig. 8. Sites (1), (2) and (3) are representative sites of fault-slip stress inversions performed by Arancibia et al. (1999) along the LOFS eastern master fault. Sites A and B correspond to epicentral location of the main events ($M_w = 6.1$ and $M_w = 6.2$ respectively) of the Aysén seismic swarm (Legrand et al., 2011), the largest seismic events ever recorded for the LOFS. Site C represents the Hudson $M_w = 6.0$ event, documented by Lange et al. (2008) and references therein.

els by using a Mohr–Coulomb yield criterion. Therefore, it produces a highly discontinuous stress and strain fields throughout the fault zone vicinity. However, mylonitic shear bands are distributed within a large width in contrast to a discrete plane, as can be seen in Cembrano et al. (2002). Also, in numerical simulations of obliquely convergent plate boundaries (e.g. Braun and Beaumont, 1995), deformation localizes in wide shear zones within a transpressional tectonic regime.

5.2. Consistency between the model and geological/seismic observations

To assess the validity, advantages and limitations of the proposed model, we compare our results with field data found in the literature (Fig. 8). Specifically, we confront our results with fault slip data inversions and crustal seismicity obtained from local and/or regional networks (Arancibia et al., 1999; Lange et al., 2008; Legrand et al., 2011). We highlight that both data sources are restricted to the brittle portion of the lithosphere. However, the brittle domain of a fault zone should slip as a response to the flow of the stronger brittle–plastic transition domain (Mancktelow, 2006), where the localization or distribution of brittle fracturing strongly depend on the underlying lithosphere low or high viscosity, respectively (Schueller et al., 2005). Therefore, if we consider long-term deformation, comparing the model stress state with fault slip data and crustal seismicity should be valid as a first order approximation, given that individual faults respond to the fault zone stress calculated in this model.

To confront our model with available seismic data, we project the 10 km-depth modeled stress tensor on the nodal plane solu-

mechanisms, with the aim of achieving a more complete understanding of the fault zone behavior (Kohlstedt et al., 1995).

Previous efforts to study the LOFS stress field, such as in Islam (2009), considered fault zones as individual lines in 2D mod-

Table 1

Comparison between seismic data (Lange et al., 2008; Legrand et al., 2011) and model results. Vectors are given in azimuth/plunge degrees.

Site	Seismic data (s)	Model results (τ)	Missfit (°)
A	129/45	145/43	12
B	179/09	173/18	9.4
C	191/22	189/19	4

tion evaluated for three representative seismic events. To this end, we compute the modeled shear stress vector τ

$$\tau = \sigma n - (n \cdot \sigma n)n. \tag{9}$$

where σ is the modeled stress tensor and n is the nodal plane solution in the seismic events. Projecting τ onto the slip s recorded in an earthquake at the location of its nucleation, we calculate the misfit angle between both vectors (Table 1). A small misfit of 4° to 12° is confirmed for the three seismic events studied.

Following this, we compare the 10 km-depth modeled stresses with the paleostress inversion from structural field measurements. It is important to remark that both our model and fault slip inversions describe the long-term averaged stress during a certain tectonic period. We calculate the misfit between paleostress inversion and modeled σ_1 orientations and ϕ values (Table 2). The similar values observed indicate that the bulk stressing on the fault zone calculated in this model is capable and sufficient to approximately reproduce the state of stress ellipticity on shallower portions of the crust. Moreover, it also suggests that the stress regime has not changed much since the brittle deformation took place, that is from 1.6 Ma (Lavenu and Cembrano, 1999).

Although earthquakes represent an instantaneous event of deformation, we remark that these events (and particularly the Aysén 2007 seismic swarm) nucleated upward from the brittle–plastic transition. Furthermore, there is a low misfit angle (4°–12°) between modeled and seismic slip vectors. This indicates that the model is sufficiently accurate in predicting the deformation and stress styles at the fault zone, regardless of the rheological difference between these structural levels. However, a different stress shape ratio distribution can be observed in the 15 km-depth model (Fig. 6). Secondary faults exhibit a less extensional-to-transtensional behavior than the 10 km-depth model, being loaded mostly in transtensional-to-strike-slip in the 15 km-depth model. This indicates that the mode of fracturing (and therefore, focal mechanism of earthquakes if they are generated) varies in higher depths of the brittle–plastic transition.

5.3. Tectonic insights

As shown in Fig. 4, the predicted maximum principal stress orientation within the forearc and foreland is not parallel to the convergence vector, but it is clockwise rotated from the convergence vector by 5° to 19°, whereas at the fault zone it is rotated up to 25° counter-clockwise. The results in the fault zone are consistent with analytical solutions for the velocity fields in oblique convergence margins (Teyssier et al., 1995) and geological studies

in the northern end of the LOFS (Pérez-Flores et al., 2016), which implies that the oblique component of convergence is mostly accommodated by a margin parallel fault system. In fact, Teyssier et al. (1995) propose that this partitioning is likely due to the convergence velocity and its obliquity rather than the mechanical properties of the lithosphere. However, modeling shear zones without any contrast in elasticity modulus or yield stress would produce a fully non-partitioned stress field. Thus, we conclude that both the spatial distribution of rheological heterogeneities and the convergence velocity/obliquity determine the stress distribution within the continental margin.

Stress states are heterogeneous within different fault segments of the duplex (Fig. 6), whereas the single fault model under the same boundary conditions and rheological properties displays only a pure strike-slip shearing mode ($\phi \approx 0.5$). Therefore, the orientation of the plastic shear zone plays a key role in how the fault is loaded. The eastern master fault displays stresses close to pure strike-slip shearing mode ($\phi = 0.45$–0.5), whereas the western fault loads mostly compressional-to-transpressional shearing mode ($\phi \approx 0.2$), which is consistent with geomorphologic, block uplifting observations and BEM modeling (Thomson, 2002; Glasser and Ghiglione, 2009; Stanton-Yonge et al., 2016). In fact, the western master fault accommodates the compressional stress arising from convergence, thus allowing the uplifting of the Cordillera at the considered latitude. Also, the disruption of the stress field near a fault intersection, which is caused by the adjacent faults' kinematics must be taken into account. For instance, transtensional-to-extensional behavior of NE-secondary-faults is limited to their easternmost segment, most likely due to the feedback between their kinematics and the eastern master fault strike-slip kinematics. This feedback was also observed in the Aysén seismic swarm where the extensional $M_w = 6.1$ event (A in Fig. 1) triggered the following strike-slip $M_w = 6.2$ (B in Fig. 1) event in the eastern master fault (Legrand et al., 2011).

The stress state contrast between the 10 km-model and the 15 km-model can be explained by the change in boundary conditions of the model. The 15 km-model displays, in overall, a stress state shifted towards compressional loading of both the eastern and western master faults. In this scenario, both vertical and NS-trending stress boundary conditions, given by lithostatic pressure, increase in the same magnitude. However, the identical velocity boundary conditions between both models implies that EW-trending stress increases in depth. Since stress is equally magnified for two orthogonal directions (vertical and NS-trending) in depth, it requires a greater stress component in the remaining orthogonal direction (EW-trending) to produce the same level of deformation. In this context, secondary faults diminish their extensional behavior, which is due to the increase of σ_1 (horizontal) versus vertical stress. Furthermore, rotations of the stress tensor in the model are invariant between the two models, given that the faults and boundary condition orientations remain constant. In this regard, the variation in depth of the topography's influence, faults' dip and the relative velocity of the subduction interface, should account for the stress tensor rotation.

Table 2

Comparison between observed data in Paleostress inversions performed by Arancibia et al. (1999) and modeled data. The model results were averaged within a range of 500 m of the paleostress inversion site location and the paleostress inversion was averaged considered the number of fault planes measured in-situ.

Site	σ_1 orientation			ϕ value		
	Paleostress inversion	Model	Misit	Paleostress inversion	Model	Difference of averages
1	087/01	070/00	15.7	0.03–0.29	0.42–0.45	−0.299
2	096/12	094/04	15.2	0.52–0.54	0.41–0.62	0.017
3	250/07	070/01	8.5	0.3–0.5	0.32–0.45	0.033

Fault slip rates predicted by our analysis are comparable and consistent with similar mechanical models at a larger scale. Whereas BEM models fault zones as discrete surfaces (e.g. Stanton-Yonge et al., 2016), following the theory of angular dislocation in an elastic medium, our model takes into account the inner rheology of fault zones within a given width. It considers that deformation compartmentalizes on the entire fault zone volume. The advantages of the FE model are that we can model with a greater level of detail small-scale geologic features, resulting in more accurate mechanics of fault slip. Further, the consideration of elasto-plastic rheology on the fault zone represents the velocity upper bound expected within the brittle regime of the overlying lithosphere. Although, brittle deformation is partitioned into imbricated discrete faults, each of which should slip at slower rates than their brittle–plastic counterpart.

The slip rate (16.6 mm/yr) calculated in the single fault model is compartmentalized within the LOFS duplex. It can be observed in Fig. 7 that the southernmost single segment of the LOFS displays a value of 16 mm/yr, which indicates that it sustains most of the equivalent slip of the single-fault model. However, as the duplex extends from south to north, its overall slip rate is shared between both master faults: the slip rate of the eastern master fault increases progressively to the north, whereas that of the western master fault decreases. This observation can be explained by their stress loading mode. The southernmost segment of the western fault is loaded under transpressional-to-strike-slip shearing mode, thus sustaining a significant fraction of the margin-parallel component of the convergence vector. In contrast, the northernmost segment of the westernmost is loaded in a transpressional-to-compressional shearing mode. This fact, along with its steep dip, suggests that in the north it accommodates only the margin-orthogonal component of the convergence vector. Furthermore, this vertical slip rate of 2 mm/yr could be significant to the pop-up blocks uplifting, and to the orogenesis at this latitude.

It can be observed in Fig. 7 that the slip rate field is not smooth throughout all of the master faults' segments. Slip rate in the eastern master fault is disrupted by the presence of oblique NE-striking faults. Moreover, the magnitude of the slip rate is higher at the northern segments of fault intersections in contrast to southern segments. This phenomenon can also be explained if we consider the $M_w = 6.1$ and 6.2 events of the Aysén swarm: when the extensional $M_w = 6.1$ event occurred, it displaced the northern block of the fault northward and the southern block southward. Thus, the velocity tendency is greater in the northern block (where the following $M_w = 6.2$ took place), given that its velocity superimposes on the dextral kinematics of the eastern master fault. On the other hand, the southern block southward velocity is in opposite sense to the eastern fault dextral kinematics. This would account for a greater overall slip rate northward of the fault intersection within the eastern master fault, rather than southward. Therefore, this example can account for the influence of coupled kinematics at adjacent fault segments on their slip rates along strike. This can be observed at Fig. 7 in the eastern master fault, where the slip rate diminishes as it moves north towards a fault intersection with a secondary NE-striking fault, then increasing again as it progresses away northward. Next to a fault intersection, the slip is enhanced in the fault segment in which both tectonic loading and the stressing caused by slip in the same sense along an adjacent fault.

Regarding the seismicity recorded in the fault system, we highlight the consistency between the focal mechanisms, the recorded slip vector (Legrand et al., 2011), and the stress state predicted by the model (Table 1). We note that these results correspond to different depths: the hypocenter depth of the $M_w = 6.2$ event (focal mechanism B in Fig. 8) was 4 km and the model was produced at 10 km. This is consistent with a brittle–plastic transition that drives the stress state of the seismogenic region.

5.4. Magma transport

When comparing to the volcano-tectonic $M_w = 6.1$ event (focal mechanism A in Fig. 8), our numerical model results show great consistency with its stress state. Transtensional-to-extensional stress is clear within the NE-striking fault responsible for the event. The Aysén seismic swarm was recorded from a maximum depth of 8.3 km and the event A occurred at a depth of 5.3 km (Legrand et al., 2011). Moreover, the entire seismic swarm is representative of magma upward migration from the brittle–plastic transition, with fault-plane solutions that can be caused by both tectonic stress and dyke inflation. These solutions often differ considerably depending on the regional tectonic setting and the magma–wall rock interaction (Roman and Cashman, 2006). On the other hand, our model captures the stress state due to the long-term behavior of the fault system, therefore immediately before magma was transported upward. Given the model's consistent results, we propose that NE-striking faults, close to the intersection with the eastern master fault, serve as long-lived magma pathways, maintained by tectonic loading conditions. This is supported by the existence of volcanos Maca and Cay, which are approximately placed on NE-striking faults, along with several monogenetic cones (Legrand et al., 2011).

Furthermore, we calculate the fluid overpressure ratio λ required to slip given a fault's orientation, which is the percentage of fluid pressure against lithostatic vertical stress. Particularly, we seek the lower boundary of λ where slip is associated with extension in brittle faulting, either in Mode I or in Mode II fracturing. Mode I alone would require greater values of λ. Following the scheme provided in Roquer et al. (2017) and references therein, λ can be obtained by rewriting the Murrel's expansion of Griffith criterion (generalized Griffith criterion) in terms of the fluid overpressure ratio λ, the normal stress $\sigma_n = \mathbf{n} \cdot \boldsymbol{\sigma} \mathbf{n}$ and the shear stress magnitude $\tau = \|\boldsymbol{\tau}\|$, projected on the nodal planes of the $M_w = 6.1$ event:

$$\lambda = \frac{P_f}{\sigma_v} = \frac{\sigma_n + T}{\rho g z} + \frac{\tau^2}{4T \rho g z} \tag{10}$$

where P_f is the fluid pressure, σ_v the vertical loading and T the tensile strength of the rock, assumed to be equal to 4 MPa (Gudmundsson, 2011). For the NE-striking fault, the minimum value of λ is 0.83, which indicates that a magma pressure equals to at least 0.83 times the value of lithostatic vertical stress is needed to produce extension, and therefore a pathway for magma upward migration. Regarding this observation, the tectonic conditions are sufficient to develop local extension for magma to migrate upwards, with no particular assistance of magma overpressure. However, this may be an oversimplified statement because a mechanically coupled feedback between overpressure and tectonic loading should usually exist. Furthermore, the link between magmatism and fault development is addressed in other works using distributed plasticity and hydro-mechanical feedback (e.g. Gerbault et al., 2012), in which magma pressure assists fault nucleation. Consequently, shear zones localization assists magma upward migration. Given that we use a non-coupled hydro-mechanical approach, an improved comprehension between tectonics and magmatism can be used in future work by integrating this feedback. On the other hand, relatively large areas of extension are observed by the model (4–10 km^2), implying that large volumes of magma could be transported up through the brittle–plastic transition, perhaps using micro-cracks pathways within mylonites (Bauer et al., 2000; Handy and Streit, 1999).

Aside from the fault where the $M_w = 6.1$ event was generated, extensional behavior also occurs on the secondary fault zone edges, as well as in other regions of the eastern master fault. This observation could provide evidence for self-similarity between crystal–plastic mechanisms and tectonic macro-behavior, given that dilatant micro-fractures are often found within plastic shear zones boundaries. These fractures precede plastic deformation (Segall and Simpson, 1986) and serve as fluid pathways, consequently being obliterated by excessive deformation when the shear zone grows. We plan to achieve a better comprehension of such coupled phenomena in the future by dealing faults with a dynamic geometry, within the context of multi-scale plasticity models.

6. Conclusions

- Our model shows that the maximum principal stress (σ_1) orientation varies along and across strike of the continental margin. In the forearc and backarc domains, σ_1 is clockwise rotated with respect to the convergence vector (ca. $15°$), whereas it is slightly counter-clockwise rotated along the duplex master faults ($15°$–$25°$). This is consistent with continental-scale slip partitioning. Fault slip rates also vary along and across strike. The duplex eastern master fault slip rates range from 7 to 10 mm/yr (increasing northward), whereas the western master fault slip ranges from 1 to 4 mm/yr (decreasing northward). Secondary NE-striking faults show slip rates up to 3 [mm/yr].
- Different branches of the LOFS differ significantly in their stress states. The eastern master fault accommodates simple shearing, with ϕ values ranging from 0.45 to 0.5, whereas the western master fault undergoes mostly pure shearing, with $\phi \approx 0.2$. Secondary NE-striking faults exhibit transtensional-to-extensional stress regimes with ϕ values ranging from 0.75 to 0.9, being the most favorable faults for magma migration, particularly close to the intersection with the eastern master fault.
- Secondary NE-striking faults of the LOFS duplex exhibit transtensional-extensional stress regimes when they are close to the eastern master fault, and not along their entire extent. Also, a fault segment will have higher slip rate in regions where both tectonic loading and local kinematics favor a compatible slip sense.
- Model results (stress orientation, ellipticity and spatial distribution) are consistent with long-term geologic observations at the outcrop scale, short-term crustal seismicity and regional tectonics in the Southern Volcanic Zone. This shows the potential of FE models to reproduce natural tectonic processes, and more importantly, demonstrates that geological and geophysical observations can be accounted for by a small number of key first order boundary conditions.

Acknowledgements

References

Angermann, D., Klotz, J., Reigber, C., 1999. Space-geodetic estimation of the Nazca–South America Euler vector. Earth Planet. Sci. Lett. 171, 329–334. http://dx.doi.org/10.1016/S0012-821X(99)00173-9.

Arancibia, G., Cembrano, J., Lavenu, A., 1999. Transpresión dextral y partición de la deformación en la Zona de Falla Liquiñe–Ofqui, Aisén, Chile (44–45S). Rev. Geol. Chile 26, 3–22. http://dx.doi.org/10.4067/S0716-02081999000100001.

Argus, D.F., Gordon, R.G., Heflin, M.B., Ma, C., Eanes, R.J., Willis, P., Peltier, W.R., Owen, S.E., 2010. The angular velocities of the plates and the velocity of Earth's centre from space geodesy. Geophys. J. Int. 180, 913. http://dx.doi.org/10.1111/j.1365-246X.2009.04463.x.

Barrientos, S., Vera, E., Alvarado, P., Monfret, T., 2004. Crustal seismicity in Central Chile. J. South Am. Earth Sci. 16, 759–768. http://dx.doi.org/10.1016/j.jsames.2003.12.001. http://www.sciencedirect.com/science/article/pii/S0895981104000070.

Bauer, P., Palm, S., Handy, M.R., 2000. Strain localization and fluid pathways in mylonite: inferences from in situ deformation of a water-bearing quartz analogue (norcamphor). Tectonophysics 320, 141–165. http://dx.doi.org/10.1016/S0040-1951(00)00065-2.

Braun, J., Beaumont, C., 1995. Three-dimensional numerical experiments of strain partitioning at oblique plate boundaries: implications for contrasting tectonic styles in the southern Coast Ranges, California, and central South Island, New Zealand. J. Geophys. Res., Solid Earth 100, 18059–18074. http://dx.doi.org/10.1029/95JB01683.

Cembrano, J., Hervé, F., Lavenu, A., 1996. The Liquiñe Ofqui fault zone: a long-lived intra-arc fault system in southern Chile. Tectonophysics 259, 55–66. http://dx.doi.org/10.1016/0040-1951(95)00066-6.

Cembrano, J., Lara, L., 2009. The link between volcanism and tectonics in the southern volcanic zone of the Chilean Andes: a review. Tectonophysics 471, 96–113. http://dx.doi.org/10.1016/j.tecto.2009.02.038.

Cembrano, J., Lavenu, A., Reynolds, P., Arancibia, G., López, G., Sanhueza, A., 2002. Late Cenozoic transpressional ductile deformation north of the Nazca–South America–Antarctica triple junction. Tectonophysics 354, 289–314. http://dx.doi.org/10.1016/S0040-1951(02)00388-8.

DeMets, C., Gordon, R.G., Argus, D.F., 2010. Geologically current plate motions. Geophys. J. Int. 181, 1–80. http://dx.doi.org/10.1111/j.1365-246X.2009.04491.x.

Gerbault, M., Cappa, F., Hassani, R., 2012. Elasto-plastic and hydromechanical models of failure around an infinitely long magma chamber. Geochem. Geophys. Geosyst. 13, q03009. http://dx.doi.org/10.1029/2011GC003917.

Glasser, N.F., Ghiglione, M.C., 2009. Structural, tectonic and glaciological controls on the evolution of fjord landscapes. Geomorphology 105, 291–302. http://dx.doi.org/10.1016/j.geomorph.2008.10.007.

Gudmundsson, A., 2011. Rock Fractures in Geological Processes. Cambridge University Press.

Handy, M.R., Streit, J.E., 1999. Mechanics and mechanisms of magmatic underplating: inferences from mafic veins in deep crustal mylonite. Earth Planet. Sci. Lett. 165, 271–286. http://dx.doi.org/10.1016/S0012-821X(98)00272-6. http://www.sciencedirect.com/science/article/pii/S0012821X98002726.

Hardacre, K., Cowie, P., 2003. Variability in fault size scaling due to rock strength heterogeneity: a finite element investigation. J. Struct. Geol. 25, 1735–1750.

Hervé, F., 1993. Paleozoic metamorphic complexes in the Andes of Aysén, Southern Chile (west of Occidentalia). In: Proceedings of the First Circum-Pacific and Circum-Atlantic Terrane Conference, pp. 64–65.

Hervé, F., Pankhurst, R., Drake, R., Beck, M., 1995. Pillow metabasalts in a mid-Tertiary extensional basin adjacent to the Liquiñe–Ofqui fault zone: the Isla Magdalena area, Aysén, Chile. J. South Am. Earth Sci. 8, 33–46. http://dx.doi.org/10.1016/0895-9811(94)00039-5.

Hirsch, P.B., Roberts, S.G., 1997. Modelling plastic zones and the brittle–ductile transition. Philos. Trans. R. Soc. A, Math. Phys. Eng. Sci. 355, 1991–2002. http://dx.doi.org/10.1098/rsta.1997.0101.

Hirth, G., Tullis, J., 1992. Dislocation creep regimes in quartz aggregates. J. Struct. Geol. 14, 145–159. http://dx.doi.org/10.1016/0191-8141(92)90053-Y. http://www.sciencedirect.com/science/article/pii/019181419290053Y.

Hurtado, D.E., Ortiz, M., 2013. Finite element analysis of geometrically necessary dislocations in crystal plasticity. Int. J. Numer. Methods Eng. 93, 66–79. http://dx.doi.org/10.1002/nme.4376.

Hutton, D.H.W., 1988. Granite emplacement mechanisms and tectonic controls: inferences from deformation studies. Earth Environ. Sci. Trans. R. Soc. Edinb. 79, 245255. http://dx.doi.org/10.1017/S0263593300014255.

Introcaso, A., Pacino, M., Fraga, H., 1992. Gravity, isostasy and Andean crustal shortening between latitudes 30 and 35°S. Tectonophysics 205, 31–48. http://dx.doi.org/10.1016/0040-1951(92)90416-4. http://www.sciencedirect.com/science/article/pii/0040195192904164.

Islam, M.R., 2009. Origin of the regional stress field along the Liquiñe–Ofqui Fault Zone (LOFZ), Southern Chilean Andes by means of FE simulation. J. Mt. Sci. 6, 1–13. http://dx.doi.org/10.1007/s11629-009-0253-x.

Karaoğlu, Ö., Browning, J., Bazargan, M., Gudmundsson, A., 2016. Numerical modelling of triple-junction tectonics at Karlóva, Eastern Turkey, with implications for regional magma transport. Earth Planet. Sci. Lett. 452, 157–170. http://

dx.doi.org/10.1016/j.epsl.2016.07.037. http://www.sciencedirect.com/science/article/pii/S0012821X16303934.

Kendrick, E., Bevis, M., Smalley Jr., R., Brooks, B., Vargas, R.B., Laura, E., Fortes, L.P.S., 2003. The Nazca South America Euler vector and its rate of change. J. South Am. Earth Sci. 16, 125–131. http://doi.org/10.1016/S0895-9811(03)00028-2. http://www.sciencedirect.com/science/article/pii/S0895981103000282.

Kohlstedt, D.L., Evans, B., Mackwell, S.J., 1995. Strength of the lithosphere: constraints imposed by laboratory experiments. J. Geophys. Res., Solid Earth 100, 17587–17602. http://dx.doi.org/10.1029/95JB01460.

Lange, D., Cembrano, J., Rietbrock, A., Haberland, C., Dahm, T., Bataille, K., 2008. First seismic record for intra-arc strike-slip tectonics along the Liquiñe–Ofqui Fault Zone at the obliquely convergent plate margin of the Southern Andes. Tectonophysics 455, 14–24. http://dx.doi.org/10.1016/j.tecto.2008.04.014. http://www.sciencedirect.com/science/article/pii/S0040195108001753.

Lara, L., Cembrano, J., Lavenu, A., 2008. Quaternary vertical displacement along the Liquiñe-Ofqui Fault Zone: differential uplift and coeval volcanism in the Southern Andes? Int. Geol. Rev. 50, 975–993. http://dx.doi.org/10.2747/0020-6814.50.11.975.

Lavenu, A., Cembrano, J., 1999. Compressional- and transpressional-stress pattern for Pliocene and quaternary brittle deformation in fore arc and intra-arc zones (Andes of Central and Southern Chile). J. Struct. Geol. 21, 1669–1691. http://dx.doi.org/10.1016/S0191-8141(99)00111-X.

Legrand, D., Barrientos, S., Bataille, K., Cembrano, J., Pavez, A., 2011. The fluid-driven tectonic swarm of Aysen Fjord, Chile (2007) associated with two earthquakes (Mw = 6.1 and Mw = 6.2) within the Liquiñe–Ofqui Fault Zone. Cont. Shelf Res. 31, 154–161. http://dx.doi.org/10.1016/j.csr.2010.05.008. http://www.sciencedirect.com/science/article/pii/S0278434310001743.

Mancktelow, N.S., 2006. How ductile are ductile shear zones? Geology 34, 345–348. http://dx.doi.org/10.1130/G22260.1. http://geology.gsapubs.org/content/34/5/345.abstract. http://geology.gsapubs.org/content/34/5/345.full.pdf+html.

McClay, K.R., 1977. Pressure solution and coble creep in rocks and minerals: a review. J. Geol. Soc. 134, 57–70. http://dx.doi.org/10.1144/gsjgs.134.1.0057. http://jgs.lyellcollection.org/content/134/1/57.abstract. http://jgs.lyellcollection.org/content/134/1/57.full.pdf+html.

Melnick, D., Rosenau, M., Folguera, A., Echtler, H., 2006. Neogene tectonic evolution of the Neuquén Andes western flank (3739s). Spec. Pap., Geol. Soc. Am. 407, 73–95. http://dx.doi.org/10.1130/2006.2407(04). http://specialpapers.gsapubs.org/content/407/73.abstract. http://specialpapers.gsapubs.org/content/407/73.full.pdf+html.

Métois, M., Socquet, A., Vigny, C., 2012. Interseismic coupling, segmentation and mechanical behavior of the Central Chile subduction zone. J. Geophys. Res., Solid Earth 117, b03406. http://dx.doi.org/10.1029/2011JB008736.

Moreno, M., Melnick, D., Rosenau, M., Bolte, J., Klotz, J., Echtler, H., Baez, J., Bataille, K., Chen, J., Bevis, M., Hase, H., Oncken, O., 2011. Heterogeneous plate locking in the South–Central Chile subduction zone: building up the next great earthquake. Earth Planet. Sci. Lett. 305, 413–424. http://dx.doi.org/10.1016/j.epsl.2011.03.025. http://www.sciencedirect.com/science/article/pii/S0012821X11001695.

Nakamura, K., Jacob, K.H., Davies, J.N., 1977. Volcanoes as possible indicators of tectonic stress orientation – Aleutians and Alaska. Pure Appl. Geophys. 115, 87–112. http://dx.doi.org/10.1007/BF01637099.

Pérez-Flores, P., Cembrano, J., Sánchez-Alfaro, P., Veloso, E., Arancibia, G., Roquer, T., 2016. Tectonics, magmatism and paleo-fluid distribution in a strike-slip setting: insights from the northern termination of the Liquiñe–Ofqui fault system, Chile. Tectonophysics 680, 192–210. http://dx.doi.org/10.1016/j.tecto.2016.05.016. http://www.sciencedirect.com/science/article/pii/S0040195116301330.

Pouya, A., Ghoreychi, M., 2001. Determination of rock mass strength properties by homogenization. Int. J. Numer. Anal. Methods Geomech. 25, 1285–1303. http://dx.doi.org/10.1002/nag.176.

Provost, A.S., Chéry, J., Hassani, R., 2003. 3D mechanical modeling of the GPS velocity field along the North Anatolian fault. Earth Planet. Sci. Lett. 209, 361–377. http://dx.doi.org/10.1016/S0012-821X(03)00099-2.

Regenauer-Lieb, K., Yuen, D., 2003. Modeling shear zones in geological and planetary sciences: solid- and fluid-thermalmechanical approaches. Earth-Sci. Rev. 63, 295–349. http://dx.doi.org/10.1016/S0012-8252(03)00038-2. http://www.sciencedirect.com/science/article/pii/S0012825203000382.

Regenauer-Lieb, K., Yuen, D.A., 1998. Rapid conversion of elastic energy into plastic shear heating during incipient necking of the lithosphere. Geophys. Res. Lett. 25, 2737–2740. http://dx.doi.org/10.1029/98GL02056.

Roman, D.C., Cashman, K.V., 2006. The origin of volcano-tectonic earthquake swarms. Geology 34, 457–460. http://dx.doi.org/10.1130/G22269.1. http://geology.gsapubs.org/content/34/6/457.abstract. http://geology.gsapubs.org/content/34/6/457.full.pdf+html.

Roquer, T., Arancibia, G., Rowland, J., Iturrieta, P., Morata, D., Cembrano, J., 2017. Fault-controlled development of shallow hydrothermal systems: structural and mineralogical insights from the Southern Andes. Geothermics 66, 156–173. http://doi.org/10.1016/j.geothermics.2016.12.003. http://www.sciencedirect.com/science/article/pii/S0375650516301948.

Rubin, A.M., 1995. Propagation of magma-filled cracks. Annu. Rev. Earth Planet. Sci. 23, 287–336. http://dx.doi.org/10.1146/annurev.ea.23.050195.001443.

Sánchez, P., Pérez-Flores, P., Arancibia, G., Cembrano, J., Reich, M., 2013. Crustal deformation effects on the chemical evolution of geothermal systems: the intra-arc Liquiñe–Ofqui Fault system, Southern Andes. Int. Geol. Rev. 55, 1384–1400. http://dx.doi.org/10.1080/00206814.2013.775731.

Schmalholz, S.M., Maeder, X., 2012. Pinch-and-swell structure and shear zones in viscoplastic layers. J. Struct. Geol. 37, 75–88. http://dx.doi.org/10.1016/j.jsg.2012.01.026. http://www.sciencedirect.com/science/article/pii/S0191814112000351.

Schueller, S., Gueydan, F., Davy, P., 2005. Brittle-ductile coupling: role of ductile viscosity on brittle fracturing. Geophys. Res. Lett. 32, l10308. http://dx.doi.org/10.1029/2004GL022272.

Segall, P., Simpson, C., 1986. Nucleation of ductile shear zones on dilatant fractures. Geology 14, 56–59. http://dx.doi.org/10.1130/0091-7613(1986)14<56:NODSZO>2.0.CO;2. http://geology.gsapubs.org/content/14/1/56.abstract. http://geology.gsapubs.org/content/14/1/56.full.pdf+html.

Sibson, R.H., 1994. Crustal stress, faulting and fluid flow. Geol. Soc. (Lond.) Spec. Publ. 78, 69–84. http://dx.doi.org/10.1144/GSL.SP.1994.078.01.07. http://sp.lyellcollection.org/content/78/1/69.abstract. http://sp.lyellcollection.org/content/78/1/69.full.pdf+html.

de Souza Neto, E.A., Peric, D., Owen, D.R.J., 2011. Computational Methods for Plasticity: Theory and Applications. John Wiley & Sons.

Stanton-Yonge, A., Griffith, W.A., Cembrano, J., Julien, R.St., Iturrieta, P., 2016. Tectonic role of margin-parallel and margin-transverse faults during oblique subduction in the southern volcanic zone of the Andes: insights from boundary element modeling. Tectonics 35, 1990–2013. http://dx.doi.org/10.1002/2016TC004226.

Teyssier, C., Tikoff, B., Markley, M., 1995. Oblique plate motion and continental tectonics. Geology 23, 447–450. http://dx.doi.org/10.1130/0091-7613(1995)023<0447:OPMACT>2.3.CO;2. http://geology.gsapubs.org/content/23/5/447.abstract. http://geology.gsapubs.org/content/23/5/447.full.pdf+html.

Thomson, S.N., 2002. Late Cenozoic geomorphic and tectonic evolution of the Patagonian Andes between latitudes 42°S and 46°S: an appraisal based on fission-track results from the transpressional intra-arc Liquiñe–Ofqui Fault Zone. Bull. Geol. Soc. Am. 114, 1159–1173. http://dx.doi.org/10.1130/0016-7606(2002)114<1159:LCGATE>2.0.CO;2. http://gsabulletin.gsapubs.org/content/114/9/1159.abstract. http://gsabulletin.gsapubs.org/content/114/9/1159.full.pdf+html.

Tullis, J., Yund, R.A., 1987. Transition from cataclastic flow to dislocation creep of feldspar: mechanisms and microstructures. Geology 15, 606–609. http://dx.doi.org/10.1130/0091-7613(1987)15<606:TFCFTD>2.0.CO;2. http://geology.gsapubs.org/content/15/7/606.abstract. http://geology.gsapubs.org/content/15/7/606.full.pdf+html.

Vargas, G., Rebolledo, S., Sepúlveda, S.A., Lahsen, A., Thiele, R., Townley, B., Padilla, C., Rauld, R., Herrera, M.J., Lara, M., 2013. Submarine earthquake rupture, active faulting and volcanism along the major Liquiñe–Ofqui Fault Zone and implications for seismic hazard assessment in the Patagonian Andes. Andean Geol. 40, 141–171. http://dx.doi.org/10.5027/andgeoV40n1-a07. http://www.scielo.cl/scielo.php?script=sci_arttext&pid=S0718-71062013000100007&nrm=iso.

Voce, E., 1955. A practical strain-hardening function. Metallurgia 51, 219–226.

Wang, K., Hu, Y., Bevis, M., Kendrick, E., Smalley, R., Vargas, R.B., Laura, E., 2007. Crustal motion in the zone of the 1960 Chile earthquake: detangling earthquake-cycle deformation and forearc-sliver translation. Geochem. Geophys. Geosyst. 8, q10010. http://dx.doi.org/10.1029/2007GC001721.

White, S., Burrows, S., Carreras, J., Shaw, N., Humphreys, F., 1980. On mylonites in ductile shear zones. J. Struct. Geol. 2, 175–187. http://dx.doi.org/10.1016/0191-8141(80)90048-6. http://www.sciencedirect.com/science/article/pii/0191814180900486.

Woodcock, N.H., Fischer, M., 1986. Strike-slip duplexes. J. Struct. Geol. 8, 725–735. http://dx.doi.org/10.1016/0191-8141(86)90021-0.

Zienkiewicz, O.C., Taylor, R.L., 2000. The Finite Element Method: Solid Mechanics, vol. 2. Butterworth–Heinemann.